Research Article

Vibration Characteristic Analysis of a Coupling System for Compound Biaxial and Inter-Shaft Bearings

Kun Li [ID],[1,2] **Hongchang Ding** [ID],[1,3] **Guohua Cao** [ID],[1,3] **and Han Hou** [ID][1]

[1]*School of Mechanical and Electric Engineering, Changchun University of Science and Technology, Changchun 130022, China*
[2]*Engineering Training Center, Changchun Institute of Technology, Changchun 130012, China*
[3]*Chongqing Research Institute, Changchun University of Science and Technology, Chongqing 401135, China*

Correspondence should be addressed to Hongchang Ding; cclggongzuo@163.com and Guohua Cao; custcaoguohua@163.com

In order to analyse the system spatial vibration of compound biaxial and inter-shaft bearings during unbalanced excitation, the theory of rotor dynamics and bearing contact deformation are combined to establish a coupling system model of compound biaxial and inter-shaft bearings. Considering the moment of inertia, gyro effect, and structural damping, a one-dimensional beam model is used to perform the MATLAB numerical calculation of the coupling system to obtain the modal characteristics of the system, and based on the ANSYS simulation analysis of the three-dimensional model, a modal test is used to obtain the system modal shape and test frequency response function to verify the rationality of the coupling system model. Based on the Runge-Kutta iterative method and Hamilton's principle, the nonlinear amplitude-frequency response of the system is calculated while taking into account the influence of the compound biaxial eccentricity, as well as the stiffness and radial clearance of the inter-shaft bearing. The results show that the changes in the eccentricity of the compound biaxial and the structural parameters of the inter-shaft bearing cause the unbalanced excitation of the system, additional external load changes, and different coupled vibrations between the composite compound biaxial and inter-shaft bearings. Therefore, it is reasonable to match the structural parameters of the coupling system and improve the dynamic performance to avoid system resonance.

1. Introduction

In order to improve the measurement accuracy and structure compactness, a compound biaxial dual-axis and dual-drive structure has been widely used in high-precision angle metering turntables [1–3]. Due to machining accuracy, installation eccentricity, and mechanical wear, when the main shaft is running, the inertia centre line is not on the rotation centre line of the main shaft, and furthermore, there is an imbalance phenomenon. At the same time, the unbalanced force is proportional to the square of the speed. During operation, the slight fluctuation of the unbalanced amount of the system will also produce a certain centrifugal force, which will cause the unbalanced vibration of the spindle [4, 5]. In order to produce a reliable and stable angle metering turntable, it is very necessary and important to predict the dynamic characteristics of the system and to study the vibration characteristics. For the main structure of the angle metering turntable, the multi-frequency unbalanced excitation force and the vibration coupling caused by the compound biaxial and inter-shaft bearings make the system vibration problem more complicated in the coupling system [6, 7]. However, due to the structural complexity of the compound biaxial system, it is a challenge to use the traditional methods (such as transfer matrix method and modal synthesis method) to obtain the dynamic characteristics [8]. With the rapid development of computer technology, digital co-simulation analysis has become an effective method for obtaining the dynamic characteristics of complex shafting. In order to achieve the high-precision system control and angle measurement of an angle measurement turntable [9–11], scholars around the world have conducted research on the dynamic characteristics of a complex shaft system.

A team from Isfahan University of Technology performed a full dynamic analysis of a high-speed rotor with certain geometrical and mechanical properties. The analysis was carried out using a 3D finite element model, a 1D beam-type model, and an experimental modal test. The Campbell diagram, critical speeds, operational deflection shapes, and unbalanced response of the rotor were obtained in order to completely investigate the dynamic behaviour of the rotating system [12]. The French Centre National Recherche de la Scientifique (CNRS) calculated the dynamic characteristics of the corresponding rotating system by using the overall nonrotating mode of a flexible blaster-axis assembly, and CNRS verified the accuracy of the nonrotating mode formation by using the finite element cyclic symmetry method [13]. Northeastern University established a new dynamic model of rotor-blade systems considering the lateral and torsional deformations of a shaft. The following phenomena were revealed by the functional relationship between the natural frequency and the rotational speed of the rotor-blade system, and the complicated coupling modes of the rotor-blade system were obtained [14]. A team at Taiwan University studied and drew diagrams of the coupling mode shapes. In addition, the influence on the coupling vibrations of the shaft-torsion and blade-bending coupling vibrations of a multi-disk rotor system was investigated analytically [15]. Dalian Jiaotong University studied the rigid motion of the shaft of an aero-engine fan rotor system, the elastic deformation of the support structure, and the transverse motion of the shaft caused by the unbalanced mass, and the university analysed the influence on the spectrum in the subcritical and supercritical ranges [16]. The Korea Aerospace Research Institute developed the rotordynamic model of a fuel turbopump and performed a dynamic analysis to predict the rotating natural frequencies, critical speeds, and system instability [17]. Beihang University considered the intermediate bearing offset, and proposed the cross coordinate system modelling method for a dual-rotor system to address the issue that the high- and low-pressure rotors could not be modelled in the unified coordinate system due to their different motion forms, and to accurately simulate the influence law of the axial deviation of the intermediate pivot on the dynamics of the dual-rotor system [18].

In the abovementioned literature, scholars have paid more attention to the dynamic characteristics of single shaft systems and high-speed systems with double rotors and inter-shaft bearings [18–20]. There is not much theoretical research into the dynamic characteristics of high-precision composite compound biaxial and inter-shaft bearings systems. The compound biaxial structure of a high-precision angle metering turntable is an innovative configuration to ensure detection accuracy and a compact structure. The main difference between the compound biaxial structure and the traditional single shaft structure is the inter-shaft bearing used to support the external and internal shafts [3].

In this paper, we present the structure of the compound biaxial and inter-shaft bearings for high precision angular metrology turntable [1]. In Section 2, we establish the mathematical model of a coupling system for compound biaxial and inter-shaft bearings. In Section 3, we describe the numerical calculations, dynamics simulations, and modal experiments of the compound biaxial system, which verify the rationality of the coupling system model. In Section 4, we describe the research on the vibration characteristics of the coupled system for compound biaxial and inter-shaft bearings. Conclusions are provided in Section 5.

2. Modelling of Compound Biaxial Coupling System

2.1. Structural Model of Compound Biaxial Coupling System. The high-precision angular metrology turntable mainly adopts the compound biaxial structure of the inner-outer ring with reciprocal roll angles [1]. The inner shaft is supported by bearing A and inter-shaft bearing C, and the outer shaft is supported by the high-precision turntable bearing B. The turntable is mainly composed of a rigid turntable, a rigid transition turntable, a rigid outer shaft, and an elastic inner shaft. The inter-shaft bearing C is used to achieve the double shaft coupling of the inner shaft and the outer shaft, and the inner-outer double shafts are independently driven by a torque motor A and a torque motor B. In actual operation, the compound biaxial structure cannot achieve complete balance. Assuming that the initial phase angle of the unbalanced force is zero, there are two eccentricities at different positions, and the driving torques of the inner and outer shafts are defined as T1 and T2, respectively. The simplified compound biaxial system of the high-precision angular metrology turntable is shown in Figure 1.

It is assumed that the stiffness of the bearings is isotropic, and the influence of the cross-coupling stiffness of the bearing is ignored. The bearing stiffness parameter values are shown in Table 1. The mass matrix and the stiffness matrix are necessary conditions for analysing the dynamic characteristics of the system, which depends only slightly on the damping matrix. Therefore, the bearing damping terms can be ignored. The system geometric parameters and the turntable parameters are shown in Tables 2 and 3, respectively.

2.2. Mathematical Modelling of Compound Biaxial Coupling System. Considering the support of the inter-shaft bearing, the coupling system model of the compound biaxial and inter-shaft bearings is established, as shown in Figure 2. It is assumed that the inner shaft is a flexible shaft and the outer shaft is a rigid shaft, the two shafts continuously rotate forward and backward, and the turntable has rigid turntables I and II (only the radial vibration of the rotor is considered, and the torsion and axial vibration of the rotor are ignored). The system is described by three degrees of freedom, the model bearings A, B, and C are rolling bearings and are elastically supported, and bearing C is an inter-shaft bearing. The inner shaft is supported by bearing A and bearing C. The outer shaft is independently supported by bearing B. Thus, *o-xyz* is the coordinate system of the component to be inspected that is affixed to the inner axis, and *O-XYZ* is the fixed coordinate system of the base (ground) of the turntable.
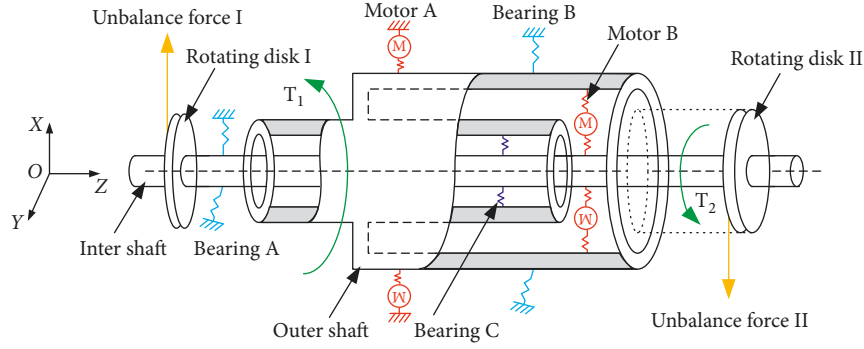
FIGURE 1: Structural model of compound biaxial system. Rotating disk I is a polyhedron. Rotating disk II is the circular dividing part to be inspected. Bearing A is a ball bearing and Bearing B is a turntable bearing. Bearing C is a dense ball bearing. Motor A and Motor B are torque motors.

TABLE 1: Bearing radial stiffness.

Bearing	A	B	C
Radial stiffness(N/m)	6.11×10^8	5.02×10^6	6.03×10^8

TABLE 2: Geometric properties of the biaxial shaft.

Geometric properties	Length (mm)	Inner diameter (mm)	Outer diameter (mm)
Inner shaft	198	0	20
Outer shaft	146	24/160	40/180

TABLE 3: Rotating disk data.

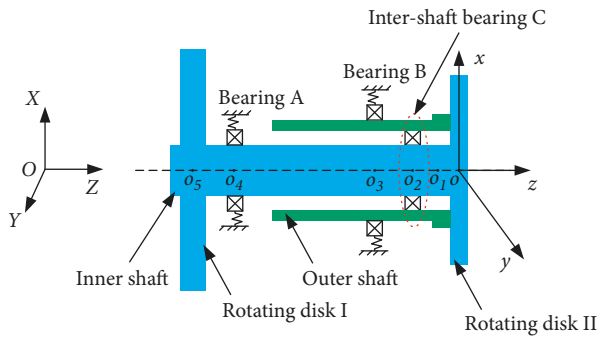| Data properties	I	II
Mass (kg)	0.2	0.2
J_d (kgm^2)	4.0×10^{-5}	1.0×10^{-4}
J_p (kgm^2)	2.0×10^{-5}	5.0×10^{-5}

FIGURE 2: Coupling system model of compound biaxial and inter-shaft bearing. The blue shaft is the inner shaft. The green shaft is the outer shaft. O is the mass centre of the item to be inspected. O_1 is the mass centre of the turntable. O_2 is the mass centre of the inter-shaft bearing. O_3 is the mass centre of rotary table bearing. O_4 is the mass centre of the inner shaft ball bearing. O_5 is the mass centre of the polyhedron.

2.2.1. Motion Equation of Compound Biaxial Coupling System.
By using the coupling system of compound biaxial and inter-shaft bearings, combined with the classical Lagrange equation (20)–(22):

$$\frac{d}{dt}\left[\frac{\partial L}{\partial \dot{r}}\right] - \frac{\partial L}{\partial r} + \frac{\partial D}{\partial \dot{r}} = F(t). \tag{1}$$

where L is the Lagrange function of the system (the difference between the kinetic energy and the potential energy of the system), D is the dissipated energy of the system, r is the generalized coordinate vector (the displacement vector of the system), and $F(t)$ is the generalized external force acting on the system for which the centrifugal force function is caused by the unbalanced excitation.

After substituting the kinetic energy, potential energy, and dissipated energy of the compound biaxial rotating disk into the Lagrange equation, in the system coordinate system, the differential equation of motion of the rotating disk of the compound biaxial coupling system is as follows:

$$\mathbf{M_i}\ddot{r}_i + \left(\Omega \mathbf{G_i} + \mathbf{C_i} + \mathbf{C_{a,i}}\right)\dot{r}_i + \left(\mathbf{K_i} + \dot{\Omega}\mathbf{K_i} + \mathbf{K_{a,i}}\right)\mathbf{r_i}$$
$$= \mathbf{F_{u,i}} + \mathbf{F_{g,i}} + \mathbf{F_{c,i}} + \mathbf{F_{a,i}}. \tag{2}$$

In the above equations, $\mathbf{M_i}$, $\mathbf{C_i}$, $\mathbf{G_i}$, and $\mathbf{K_i}$ are the mass matrix, damping matrix, gyro matrix, and structural stiffness matrix of the rotating disk of the compound biaxial system, respectively, the effects of the variable speed of rotation Ω are considered in the stiffness matrix, $\mathbf{F_{u,i}}$ and $\mathbf{F_{g,i}}$ are the mass unbalance force and the gravity force vector acting on the rotating disk, respectively, the external force vector $\mathbf{F_{c,i}}$ represents the bearing contact forces. $\mathbf{C_{a,i}}$, $\mathbf{K_{a,i}}$, and $\mathbf{F_{a,i}}$ are the additional damping matrix, additional stiffness matrix, and additional excitation load force vector generated on the rotating disk when the turntable rotates, respectively.

This expression is combined with the coupling system of the compound biaxial and inter-shaft bearings, in which,

$$
\mathbf{M_i} = \begin{bmatrix} m_i & 0 & 0 & 0 \\ 0 & m_i & 0 & 0 \\ 0 & 0 & I_{d,i} & 0 \\ 0 & 0 & 0 & I_{d,i} \end{bmatrix},
$$

$$
\mathbf{C_i} = \begin{bmatrix} c_{t,i} & 0 & 0 & 0 \\ 0 & c_{t,i} & 0 & 0 \\ 0 & 0 & c_{r,i} & 0 \\ 0 & 0 & 0 & c_{r,i} \end{bmatrix},
$$

$$
\mathbf{G_i} = \begin{bmatrix} 0 & 0 & 0 & 0 \\ 0 & 0 & 0 & 0 \\ 0 & 0 & 0 & I_{\rho,i}\omega_i \\ 0 & 0 & -I_{\rho,i}\omega_i & 0 \end{bmatrix},
$$

$$
\mathbf{C_{a,i}} = \begin{bmatrix} 0 & -2m_i\dot{\theta}_{a,z} & 0 & 0 \\ 2m_i\dot{\theta}_{a,z} & 0 & 0 & 0 \\ 0 & 0 & 0 & 0 \\ 0 & 0 & 0 & 0 \end{bmatrix},
$$

$$
\mathbf{K_i} = \begin{bmatrix} k_i & 0 & 0 & 0 \\ 0 & k_i & 0 & 0 \\ 0 & 0 & k_i & 0 \\ 0 & 0 & 0 & k_i \end{bmatrix},
$$

$$
\mathbf{K_{a,i}} = \begin{bmatrix} -m_i\left(\dot{\theta}^2_{a,y} + \dot{\theta}^2_{a,z}\right) & m_i\left(\dot{\theta}_{a,x}\dot{\theta}_{a,y} - \dot{\theta}^2_{a,z}\right) & 0 & 0 \\ m_i\left(\dot{\theta}_{a,x}\dot{\theta}_{a,y} - \dot{\theta}^2_{a,z}\right) & -m_i\left(\dot{\theta}^2_{a,x} + \dot{\theta}^2_{a,z}\right) & 0 & 0 \\ 0 & 0 & 0 & 0 \\ 0 & 0 & 0 & 0 \end{bmatrix},
$$

$$
\mathbf{F_{u,i}} = \begin{bmatrix} m_i e_i \omega_i^2 \cos\left(\omega_i t + \varphi_{i,0}\right) & m_i e_i \omega_i^2 \sin\left(\omega_i t + \varphi_{i,0}\right) & 0 & 0 \end{bmatrix}^{\mathrm{T}},
$$

$$
\mathbf{F_{a,i}} = \begin{bmatrix} -m_i z_i\left(\dot{\theta}_{a,x}\dot{\theta}_{a,z} + \ddot{\theta}_{a,y}\right) \\ -m_i z_i\left(\dot{\theta}_{a,y}\dot{\theta}_{a,z} - \ddot{\theta}_{a,x}\right) \\ I_i\ddot{\theta}_{a,x} - \omega_i I_{\rho,i}\dot{\theta}_{a,y} \\ \omega_i I_{\rho,i}\dot{\theta}_{a,x} - I_i\ddot{\theta}_{a,y} \end{bmatrix},
$$

$$
\Omega = \begin{bmatrix} \omega_x \\ \omega_y \\ \omega_z \\ 0 \end{bmatrix},
$$

$$
\mathbf{F_{c,i}} = \begin{bmatrix} F_{c,i} & 0 & 0 & 0 \\ 0 & F_{c,i} & 0 & 0 \\ 0 & 0 & F_{c,i} & 0 \\ 0 & 0 & 0 & F_{c,i} \end{bmatrix}.
$$

(3)

In addition, m_i is the mass of the rotating disk; $I_{d,i}$ and $I_{\rho,i}$ are the diameter moment inertia and the polar moment inertia of the rotating disk, respectively; and $c_{t,i}$ and $c_{r,i}$ are the translational damping and rotational damping of the rotating disk relative to the shaft, respectively. ω_i is the speed of the rotating disk relative to the shaft, k_i is the stiffness of the rotating disk relative to the shaft, e_i is the eccentricity of the rotating disk, and $\varphi_{i,0}$ is the initial phase angle of the unbalance of the rotating disk. $\dot{\theta}_{a,x}$, $\dot{\theta}_{a,y}$, and $\dot{\theta}_{a,z}$ are the additional angular velocity of the rotating disk relative to the x, y, and z axes in the system coordinate system, respectively. $\ddot{\theta}_{a,x}$, $\ddot{\theta}_{a,y}$, and $\ddot{\theta}_{a,z}$ are the additional angular acceleration of the rotating disk relative to the x, y, and z axes in the system coordinate system, respectively, the external force $F_{c,i}$ represent the bearing contact forces.

It is assumed that the mass of the compound biaxial system is concentrated, the influence of the radial vibration (that is, the displacement and velocity in the x and y directions) is considered, and the influence of the axial vibration is ignored. The inner shaft is a flexible shaft and the outer shaft is a rigid shaft. Based on the analysis and arrangement of the differential equation of the motion of the rotating disk in the system coordinate system, the dynamics equation of the coupled system of the compound biaxial rotating shaft can be obtained:

$$
\mathbf{M}\ddot{S} + (\mathbf{C} + \mathbf{G} + \mathbf{C_a})\dot{S} + (\mathbf{K} + \mathbf{K_a})S = \mathbf{F_u} + \mathbf{F_g} + \mathbf{F_a}. \quad (4)
$$

In the expression,

$$
\mathbf{C_a} = \begin{bmatrix} C_{a,1} & 0 & 0 & 0 & 0 & 0 \\ 0 & C_{a,2} & 0 & 0 & 0 & 0 \\ 0 & 0 & C_{a,3} & 0 & 0 & 0 \\ 0 & 0 & 0 & C_{a,4} & 0 & 0 \\ 0 & 0 & 0 & 0 & C_{a,5} & 0 \\ 0 & 0 & 0 & 0 & 0 & C_{a,6} \end{bmatrix},
$$

$$
\mathbf{K_a} = \begin{bmatrix} K_{a,1} & 0 & 0 & 0 & 0 & 0 \\ 0 & K_{a,2} & 0 & 0 & 0 & 0 \\ 0 & 0 & K_{a,3} & 0 & 0 & 0 \\ 0 & 0 & 0 & K_{a,4} & 0 & 0 \\ 0 & 0 & 0 & 0 & K_{a,5} & 0 \\ 0 & 0 & 0 & 0 & 0 & K_{a,6} \end{bmatrix},
$$

(5)

$$
\mathbf{S} = \begin{bmatrix} \tau_1 & \tau_2 & \tau_3 & \tau_4 & \tau_5 & \tau_6 \end{bmatrix}^{\mathrm{T}},
$$

$$
\mathbf{F_u} = \begin{bmatrix} \mathbf{F_{u,1}} & \mathbf{F_{u,2}} & \mathbf{F_{u,3}} & \mathbf{F_{u,4}} & \mathbf{F_{u,5}} & \mathbf{F_{u,6}} \end{bmatrix}^{T},
$$

$$
\mathbf{F_g} = \begin{bmatrix} \mathbf{F_{g,1}} & \mathbf{F_{g,2}} & \mathbf{F_{g,3}} & \mathbf{F_{g,4}} & \mathbf{F_{g,5}} & \mathbf{F_{g,6}} \end{bmatrix}^{T},
$$

$$
\mathbf{F_a} = \begin{bmatrix} \mathbf{F_{a,1}} & \mathbf{F_{a,2}} & \mathbf{F_{a,3}} & \mathbf{F_{a,4}} & \mathbf{F_{a,5}} & \mathbf{F_{a,6}} \end{bmatrix}^{\mathrm{T}},
$$

where $\mathbf{M}$, $\mathbf{C}$, $\mathbf{G}$, and $\mathbf{K}$ are the generalized mass matrix, damping matrix, gyro matrix, and stiffness matrix of the flexible axis of the inner shaft of the compound biaxial system, respectively, $\mathbf{S}$ is the generalized coordinate vector of the internal flexible axis, $\mathbf{F_u}$ and $\mathbf{F_g}$ are the unbalanced force and the generalized force vector acting on the internal flexible axis, $\mathbf{C_a}$, $\mathbf{K_a}$, and $\mathbf{F_a}$ are the additional damping matrix, additional stiffness matrix, and additional excitation load force vector, respectively, which are generated on the rotating disk of the internal flexible axis or the bearing fulcrum when the inner and outer shafts rotate.

2.2.2. Displacement and Energy Equation of Compound Biaxial System. Using the dynamics equation of the compound biaxial coupling system, the displacement equation of the rotation axis of inner shaft at any point in the x and y directions is established:

$$\begin{cases} X_1(z,t) = \sigma_1(z)x_1(t), \\ Y_1(z,t) = \sigma_1(z)y_1(t), \end{cases} \tag{6}$$

where $\sigma_1(z)$ is the displacement function of the inner rotation axis and it represents the functional relationship between the displacement at a point on the inner rotating axis and the rotating disk.

The bending angle equation of the inner rotation axis at any point in the x and y directions:

$$\begin{cases} \phi_1(z,t) \approx \dfrac{\partial Y_1}{\partial z} = \dfrac{d\sigma_1(z)}{dz}y_1(t) = \chi_1(z)y_1(t), \\ \\ \psi_1(z,t) \approx \dfrac{\partial X_1}{\partial z} = \dfrac{d\sigma_1(z)}{dz}x_1(t) = \chi_1(z)x_1(t), \end{cases} \tag{7}$$

where $\chi_1(z)$ is the curvature change function of the inner rotation axis.

The displacement equation of the outer rotation axis at any point in the x and y directions is established:

$$\begin{cases} X_2(z,t) = \sigma_2(z)x_2(t), \\ Y_2(z,t) = \sigma_2(z)y_2(t), \end{cases} \tag{8}$$

where $\sigma_2(z)$ is the displacement function of the outer rotation axis and it represents the functional relationship between the displacement at a point on the outer rotating axis and the rotating disk.

The bending angle equation of the outer rotation axis at any point in the x and y directions:

$$\begin{cases} \phi_2(z,t) \approx \dfrac{\partial Y_2}{\partial z} = \dfrac{d\sigma_2(z)}{dz}y_2(t) = \chi_2(z)y_2(t), \\ \\ \psi_2(z,t) \approx \dfrac{\partial X_2}{\partial z} = \dfrac{d\sigma_2(z)}{dz}x_2(t) = \chi_2(z)x_2(t), \end{cases} \tag{9}$$

where $\chi_2(z)$ is the curvature change function of the outer rotation axis.

The rigid rotation axis is always in steady motion, and the total kinetic energy T of the system is composed of the

kinetic energy T_D of the rotating disk and the kinetic energy of the rotation axis T_S, that is, $T = T_D + T_S$.

Kinetic energy T_{D1} of the inner rotating disk:

$$\begin{aligned} T_{D1} &= \frac{1}{2}m_1\left(v_{x1}^2 + v_{y1}^2\right) + \frac{1}{2}J_{D1}\left(v_{x1}^2 + v_{y1}^2\right)\chi_1^2(L_{11}) \\ &\quad + \frac{1}{2}J_{\rho1}\omega_1^2 - J_{\rho1}\omega_1 v_{x1} y_1 \chi_1^2(L_{11}) \\ &= \frac{1}{2}m_1\left(\dot{x}_1^2 + \dot{y}_1^2\right) + \frac{1}{2}J_{D1}\left(\dot{x}_1^2 + \dot{y}_1^2\right)\chi_1^2(L_{11}) \\ &\quad + \frac{1}{2}J_{\rho1}\omega_1^2 - J_{\rho1}\omega_1 \dot{x}_1 y_1 \chi_1^2(L_{11}). \end{aligned} \tag{10}$$

Kinetic energy T_{S1} of the inner rotation axis:

$$\begin{aligned} T_{S1} &= \frac{\rho_1\pi R_1^2}{2}\left(v_{x1}^2 + v_{y1}^2\right)\int_0^{L_{12}}\sigma_1^2(z)dz \\ &\quad + \frac{\rho_1 I_1}{2}\left(v_{x1}^2 + v_{y1}^2\right)\int_0^{L_{12}}\chi_1^2(z)dz + \rho_1 I_1 L_{12}\omega_1^2 \\ &\quad - 2\rho_1 I_1 \omega_1 v_{x1} y_1 \int_0^{L_{12}}\chi_1^2(z)dz \\ &= \frac{\rho_1\pi R_1^2}{2}\left(\dot{x}_1^2 + \dot{y}_1^2\right)\int_0^{L_{12}}\sigma_1^2(z)dz + \frac{\rho_1 I_1}{2}\left(\dot{x}_1^2 + \dot{y}_1^2\right) \\ &\quad \int_0^{L_{12}}\chi_1^2(z)dz + \rho_1 I_1 L_{12}\omega_1^2 - 2\rho_1 I_1 \omega_1 \dot{x}_1 y_1 \int_0^{L_{12}}\chi_1^2(z)dz \,. \end{aligned} \tag{11}$$

where m_1 is the mass of the inner rotating disk, v_{x1} and v_{y1} are the linear velocities of the inner rotating disk in the x and y directions, J_{D1} and $J_{\rho1}$ are the diameter moment of inertia and the polar moment of inertia for the inner rotating disk, ω_1 is the rotation speed of the inner rotation axis, ρ_1 is the density of the inner rotation axis, R_1 is the radius of the inner rotation axis, and I_1 is the inertia moment of the inner rotation axis relative to the theoretical central axis. L_{11} is the distance from point O to point O_5, and L_{12} is the distance from point O_1 to point O in the system frame.

The kinetic energy T_{D2} of the outer rotating disk is:

$$\begin{aligned} T_{D2} &= \frac{1}{2}m_2\left(v_{x2}^2 + v_{y2}^2\right) + \frac{1}{2}J_{D2}\left(v_{x2}^2 + v_{y2}^2\right)\chi_1^2(L_{21}) + \frac{1}{2}J_{\rho2}\omega_2^2 \\ &\quad - J_{\rho2}\omega_2 v_{x2} y_2 \chi_2^2(L_{21}) \\ &= \frac{1}{2}m_2\left(\dot{x}_2^2 + \dot{y}_2^2\right) + \frac{1}{2}J_{D2}\left(\dot{x}_2^2 + \dot{y}_2^2\right)\chi_1^2(L_{21}) \\ &\quad + \frac{1}{2}J_{\rho2}\omega_2^2 - J_{\rho2}\omega_2 \dot{x}_2 y_2 \chi_2^2(L_{21}). \end{aligned} \tag{12}$$

The kinetic energy T_{S2} of the outer rotation axis is:

$$T_{S2} = \frac{\rho_2 \pi \left(R_{22}^2 - R_{21}^2\right)}{2}\left(v_{x2}^2 + v_{y2}^2\right)\int_{L_{22}}^{L_{23}} \sigma_2^2(z)dz$$

$$+ \frac{\rho_2 I_2}{2}\left(v_{x2}^2 + v_{y2}^2\right)\int_{L_{22}}^{L_{23}} \chi_2^2(z)dz + \rho_2 I_2 (L_{23} - L_{22})\omega_1^2$$

$$- 2\rho_2 I_2 \omega_2 v_{x2} y_2 \int_{L_{22}}^{L_{23}} \chi_2^2(z)dz$$

$$= \frac{\rho_2 \pi \left(R_{22}^2 - R_{21}^2\right)}{2}\left(\dot{x}_2^2 + \dot{y}_2^2\right)\int_{L_{22}}^{L_{23}} \sigma_2^2(z)dz$$

$$+ \frac{\rho_2 I_2}{2}\left(\dot{x}_2^2 + \dot{y}_2^2\right)\int_{L_{22}}^{L_{23}} \chi_2^2(z)dz + \rho_2 I_2 (L_{23} - L_{22})\omega_1^2$$

$$- 2\rho_2 I_2 \omega_2 \dot{x}_2 y_2 \int_{L_{22}}^{L_{23}} \chi_2^2(z)dz .$$

$$(13)$$

where m_2 is the mass of the outer rotating disk, v_{x2} and v_{y2} are the linear velocities of the outer rotating disk in the x and y directions, J_{D2} and $J_{\rho2}$ are the diameter moment of inertia and the polar moment of inertia for the outer rotating disk, ω_2 is the rotation speed of the outer rotation axis, ρ_2 is the density of the outer rotation axis, R_{21} and R_{22} are the inner radius and outer radius of the outer rotation axis, and I_2 is the inertia moment of the outer rotation axis relative to the theoretical central axis. L_{21} is the distance from point O to point O_1, L_{22} is the distance from point O to point O_4, and L_{23} is the distance from point O to point O_2 in the system frame.

According to the theory of elastic potential energy, the generalized coordinates of the inner and outer shafts are (x_1, y_1) and (x_2, y_2), and the linear stiffness coefficients of the system are k_1 and k_2. The elastic potential energies at the positions of the inner and outer rotating disks are:

$$\begin{cases} V_1 = \frac{1}{2}k_1\left(x_1^2 + y_1^2\right), \\ \\ V_2 = \frac{1}{2}k_2\left(x_2^2 + y_2^2\right). \end{cases} \quad (14)$$

According to the Ruili dissipated energy function, the damping coefficients of the inner and outer shafts are c_1 and c_2, respectively, and the dissipated energies of the system at the positions of the inner and outer rotating disks are:

$$\begin{cases} D_1 = \frac{1}{2}c_1\left(v_{x1}^2 + v_{y1}^2\right) = \frac{1}{2}c_1\left(\dot{x}_1^2 + \dot{y}_1^2\right), \\ \\ D_2 = \frac{1}{2}c_2\left(v_{x2}^2 + v_{y2}^2\right) = \frac{1}{2}c_2\left(\dot{x}_2^2 + \dot{y}_2^2\right). \end{cases} \quad (15)$$

2.2.3. Bearing Force Equation of Inter-Shaft Bearing.

The function of the inter-shaft bearing is to connect the "inner-outer" double shaft. The inner raceway of the inter-shaft
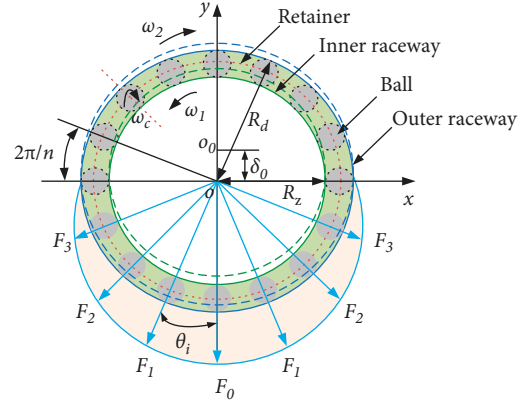

FIGURE 3: Force diagram of inter-shaft dense ball bearing. Solid lines are ideal bearings. Dotted lines are actual bearings with radial clearance (There is radial clearance).

bearing is in contact with the outer ring of the inner shaft, and the outer raceway is in contact with the inner ring of the outer shaft. Since the inter-shaft bearing is a dense ball bearing, the balls are arranged equidistantly between the inner and outer raceways of the cage. It is assumed that there are n supporting points between the raceways of the cage of the inter-shaft bearing (there are n balls in a single row). The force diagram of the inter-shaft bearing is shown in Figure 3.

According to the theory of the Hertz contact deformation, the bearing support reaction equation is:

$$F = K\delta^{\eta}, \quad (16)$$

where K is the contact stiffness, δ is the elastic deformation at the contact point of the inner and outer rings of the ball bearing, and η is the type of correlation coefficient of the bearing. The type of the correlation coefficient of the ball bearing is $\eta = 3/2$ and the type of the correlation coefficient of the roller bearing is $\eta = 10/9$.

In the inter-shaft bearing, the elastic support force of the ball i is expressed as:

$$F_i = K\delta_i^{\eta} H(\delta_i), \quad (17)$$

where δ_i^{η} is the elastic deformation at the contact point i of the inner and outer rings of the inter-shaft bearing, and the inter-shaft dense bead bearing is the ball bearing, namely, the coefficient $\eta = 3/2$, $H(\delta_i)$ is the Heaviside function at the contact point i of the inter-shaft bearing, and
$$H(\delta_i) = \begin{cases} 0 & (\delta_i \leq 0) \\ 1 & (\delta_i > 0) \end{cases}.$$

It is assumed that the contact deformation between a single ball and the inner and outer ring raceways of the inter-shaft bearing satisfies the theory of small deformation, and the radial elastic contact deformation of the ball i is as follows:

$$\delta_i = (x_i - x_0)\cos\theta_i + (y_i - y_0)\sin\theta_i - \delta_0, \quad (18)$$

where x_i, x_0, y_i, and, y_0 are the vertical and horizontal displacement components of the inner and outer raceways of the inter-shaft bearing, δ_0 is the radial clearance of the inter-

shaft bearing, and θ_i is the angle at the supporting point i of the inter-shaft bearing.

At a certain point, the angle at the supporting point i of the inter-shaft bearing is:

$$\theta_i = \omega_c \cdot t + \frac{2\pi}{n}(i-1), \tag{19}$$

where ω_c is the dynamic speed between the ball of the inter-shaft bearing and the cage for the ball rotation speed of the inter-shaft bearing, where $i = 1, 2, \ldots n$.

Ball rotation speed of inter-shaft bearing:

$$\omega_c = \omega \frac{R_z}{R_D + R_z}, \tag{20}$$

where ω is the relative speed of the inner shaft relative to the outer shaft for the compound biaxial structure, R_D is the radius of the outer ring raceway for the inter-shaft bearing, and R_z is the radius of the inner ring raceway for the inter-shaft bearing.

Since the inner and outer shafts of the compound biaxial structure are in continuous rotation, one clockwise and one counter clockwise, the rotation speed of the inner shaft relative to the outer shaft is:

$$\omega = \omega_D + \omega_z = \omega_1 + \omega_2, \tag{21}$$

where ω_D is the absolute speed of the cage, ω_z is the absolute speed of the ball, ω_1 is the speed of the inner shaft, and ω_2 is the speed of the outer shaft.

In the coordinate system of the inter-shaft bearing system, the force of the inter-shaft bearing during the rotation of the compound biaxial structure is:

$$\begin{cases} F_x = K_H \sum_{i=1}^{n} \left[(\delta_i)^{3/2} H\left((x_i - x_0)\cos\theta_i + (y_i - y_0)\sin\theta_i - r_0\right) \right] \cdot \cos\theta_i, \\ \\ F_y = K_H \sum_{i=1}^{n} \left[(\delta_i)^{3/2} H\left((x_i - x_0)\cos\theta_i + (y_i - y_0)\sin\theta_i - r_0\right) \right] \cdot \sin\theta_i, \end{cases} \tag{22}$$

where K_H is the Hertz contact stiffness of the inter-shaft bearing, r_0 is the radius of the raceway ring, and $r_0 = R_D - R_z$.

3. Model Verification of Compound Biaxial Coupling System

3.1. Discretization of Compound Biaxial Structure.
According to the actual structure of the high-precision angular metrology turntable, a one-dimensional beam model and a three-dimensional solid model are used to discretize the biaxial structure. The beam model uses nine Timoshenko beam elements for modelling, and considers the rotational inertia, gyroscopic effect, and structural damping for two turntable units and five support units, as shown in Figure 4(a).

In order to consider the influence of more complex geometric structures on the dynamic characteristics of the biaxial structure, the finite element model of the biaxial system is established in ANSYS Workbench using the solid element model, as shown in Figure 4(b). The elastic modulus, Poisson's ratio, and mass density of both shafts (aluminium 7A04 B) of the biaxial structure are 70 GPa, 0.3, and 2700 kg/m3, respectively. The finite element model of the biaxial structure uses Combin14 elements to simulate the bearing and the motor, which contain 13,549 elements and 55583 nodes in the 3D model. However, the 1D model has 16 elements and 11 nodes, as shown in Figure 4(a).

3.2. Modal Analysis of Compound Biaxial Structure.
Based on the dynamic equations of the compound biaxial coupling system, the 1D beam model and the 3D solid model of the compound biaxial structure are adopted, and the modal analysis of the biaxial structure is carried out using MATLAB and ANSYS Workbench. The numerical calculation for the 1D model and the simulation analysis of the 3D model for the modal shapes for the first six orders, are shown in Figures 5 and 6, respectively.

According to the first six orders of the modal formation, the vibration shapes of the two models are the same, and the change law of the overall shape formation is the same. However, due to the existence of the dense ball bearing in the middle, there is a phenomenon of coupling vibration between the inner shaft and the outer shaft, which preliminarily verifies the rationality of the coupling system model. The MATLAB numerical calculation of the coupling system model and the Workbench simulation of the 3D model are compared with the first six orders of the natural frequencies. The relative error of the fourth order of the natural frequency is the largest (the error is less than 8%). The main reason for this is that the simulation analysis ignores the coupling effect of the compound biaxial and inter-shaft bearings, which leads to an increase in the contact stiffness between the shaftings, and compared with the 1D model, the 3D model has higher stiffness characteristics.

The numerical calculation and the dynamic simulation analysis of the coupling system model are carried out under relatively ideal boundary conditions in order to consider the accuracy of the numerical calculation and the modal test under real working conditions. Therefore, in this research, a scanning laser vibrometer PSV-500-1D combined with a single-point laser vibrometer OFV-5000 is used to carry out modal tests on the compound biaxial structure, and the frequency response, unbalanced vibration, and response phase of the biaxial structure are obtained. The recording
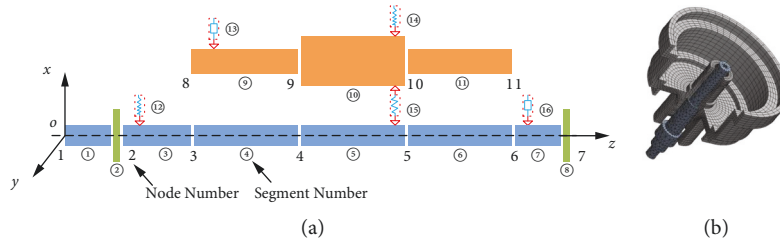
FIGURE 4: Finite element model of the compound biaxial system. (a) Beam model and (b) Solid model.
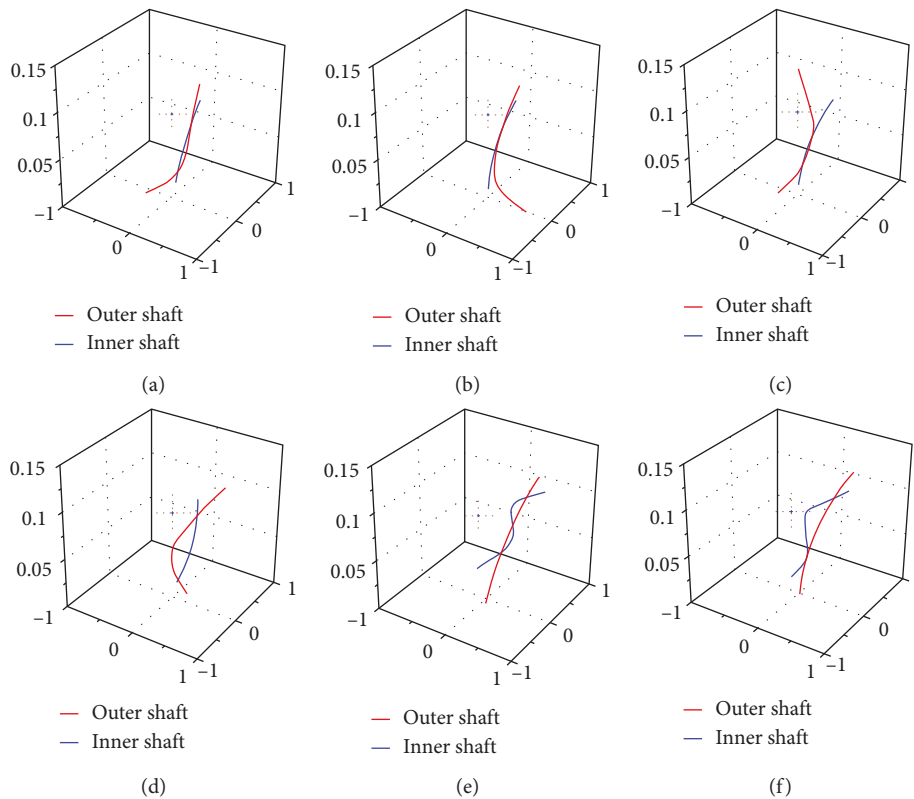

FIGURE 5: The modal shapes plotted with MATLAB. (a) Modal 1. (b) Modal 2. (c) Modal 3. (d) Modal 4. (e) Modal 5. (f) Modal 6.

and the display of the data are achieved with a PSV-500-DMS data acquisition system. The modal test is shown in Figure 7.

The excitation is applied to the end of the biaxial structure by using the turntable control system, combined with the reference signal of the single-point laser vibrometer OFV-5000. The amplitude-frequency curve of the modal test is shown in Figure 8. The amplitude-frequency curve and the natural frequency (see Table 4) are compared. The results of the modal test, numerical calculation, and finite element simulation are in good agreement, which again verifies the rationality of the coupling system model with the compound biaxial structure.

4. Vibration Characteristic Analysis of Compound Biaxial System

It is assumed that the stiffness of the bearing is isotropic, and the influence of the cross-coupling stiffness and the damping

of the bearing are ignored under ideal conditions. The eccentricity of the compound biaxial is $e0 = 0$, the stiffness and the radial clearance of the inter-shaft bearing are $KH0 = 6.03 \times 108$ N/m and $\delta 0 = 0$, respectively. According to the differential (2) of motion of the rotating disk of the compound biaxial coupling system, the excitation of the mass unbalance force and the gravity force are applied to the inner and outer rotating disks, respectively, and the excitation of the additional damping matrix, the additional stiffness matrix, and the additional load force generated on the corresponding disks are taken into account. By changing the parameters of the compound biaxial eccentricity, the stiffness and the radial clearance of the inter-shaft bearing, the vibration characteristics of the compound biaxial system are analysed.

4.1. Amplitude Frequency Response Analysis of Compound Biaxial System. In order to investigate the amplitude-frequency response of the compound biaxial system without
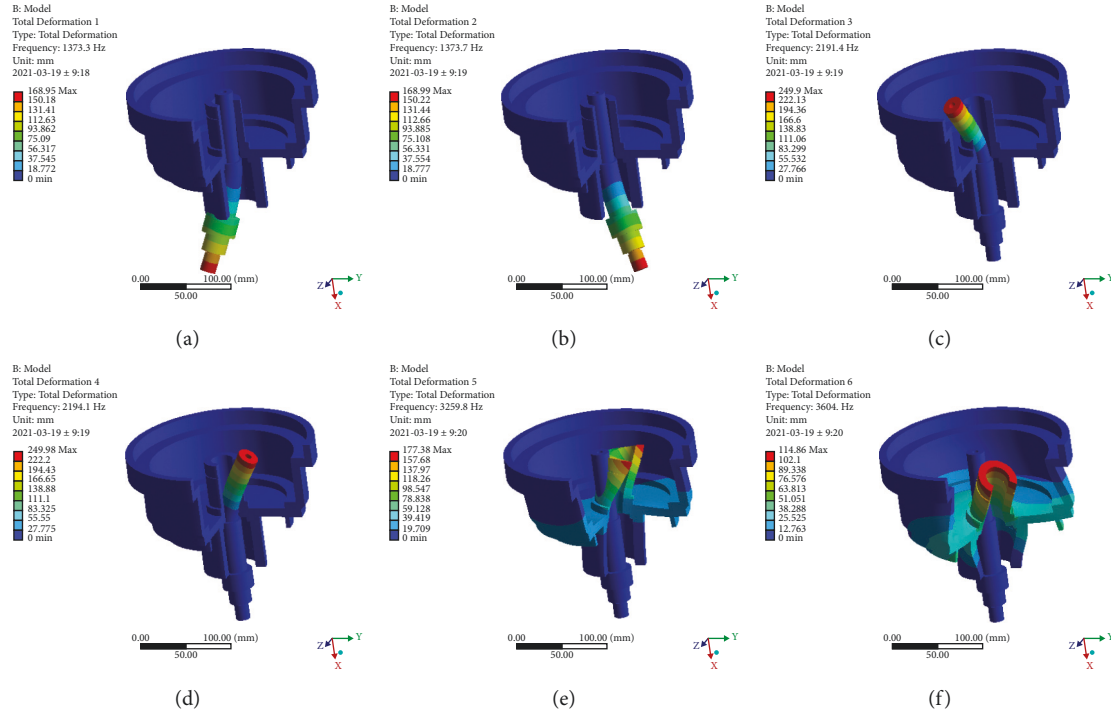
FIGURE 6: The modal shapes plotted with Workbench.

taking the influence of the dynamic load of the system into account, the differential motion (2) of the rotating disk and the dynamic (4) of the rotation axis for the compound biaxial system are numerically solved with the fourth-order Runge-Kutta iterative method. Taking the system speed as the abscissa with the amplitude-frequency curve of the compound biaxial system, the amplitude-frequency curves of the start-up and stop-down of the compound biaxial system are compared and analysed. The amplitude-frequency response curve of the compound biaxial system is near the first-order critical speed, as shown in Figure 9.

The comparative analysis of the amplitude-frequency curve of the system shows that the "inner-outer" shaft of the compound biaxial system is a continuous rotation of positive and negative reciprocals, and there are two excitation resonance peaks near the first-order critical speed during the increasing speed and decreasing speed phases of the inner and outer shafts (Increasing speed phase: the excitation resonance peak points AO1 and AO2 of the outer shaft, and the excitation resonance peak points AI1 and AI2 of the inner shaft. Decreasing speed phases: the excitation resonance peak points BO1 and BO2 of the outer shaft, and the excitation resonance peak points BI1 and BI2 of the inner shaft). The first excitation resonance is caused by the main excitation resonance of the outer shaft, the second excitation resonance is caused by the main excitation resonance of the inner shaft, and the resonant peak-peak value of the outer shaft is higher than the resonant peak-peak value of the inner shaft in the amplitude-frequency curve. Between the acceleration mutation point A and the deceleration mutation point B of the two main excitation resonance peaks of the inner shaft and the outer shaft, the double steady-state interval of the compound biaxial system is correspondingly
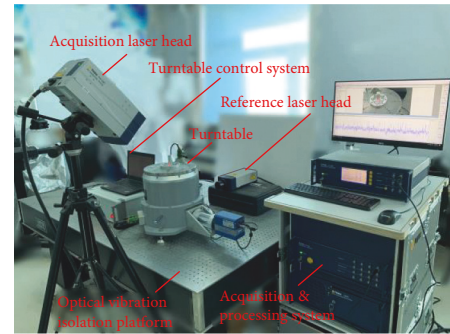

FIGURE 7: Modal test platform.

formed due to the existence of the coupling contact force and the nonlinear vibration characteristics of the rolling of the inner and outer of the inter-shaft bearing. At the same time, the double steady-state interval caused by the main excitation resonance of the inner shaft is significantly larger than that of the outer shaft. In addition, due to the coupling of the "inner-outer" shafts of the compound biaxial system, the overall trends of the two excitation resonances and the amplitude-frequency curves of the system remain the same.

4.2. Amplitude-Frequency Response Analysis of Different Eccentricity.
In order to analyse the amplitude-frequency response of the different eccentricities of the compound biaxial system, the eccentricities of the inner shaft and the outer shaft are taken as $e1 = 0.2\,\mu m$, $e2 = 0.4\,\mu m$, $e3 = 0.6\,\mu m$, and $e4 = 0.8\,\mu m$. Regardless of the influence of the dynamic
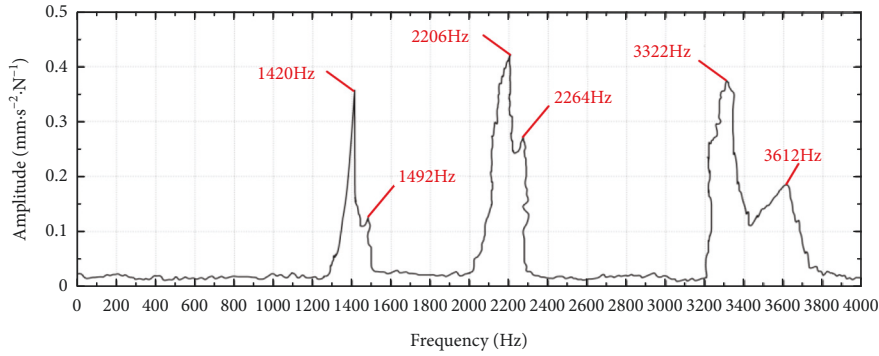
FIGURE 8: Amplitude frequency response curve of modal test.

TABLE 4: Comparison of natural frequency.

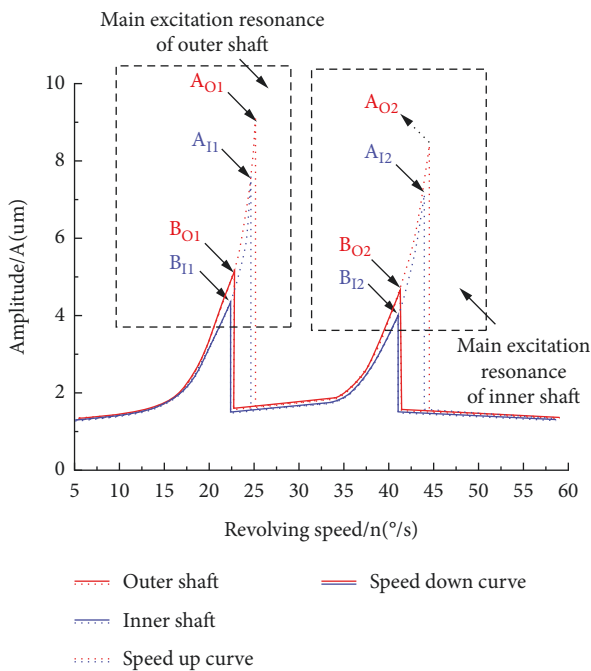| Order	Test (Hz)	MALAB results (Hz)	Workbench results (Hz)	Error (%)
1	1420	1310.266	1373.3	4.59
2	1492	1308.037	1373.7	4.78
3	2206	2085.994	2191.4	4.81
4	2264	2018.222	2191.1	7.89
5	3322	3102.026	3259.8	4.84
6	3612	3431.008	3604.0	4.89

FIGURE 9: Amplitude-frequency response curve of compound bi-axial system. Red line: outer shaft; Blue line: inner shaft; Dotted line: increasing speed curve; Solid line: decreasing speed curve.

load of the system, the equations of displacement and energy of the compound biaxial system are numerically solved by Hamilton's principle. The speed is taken as the abscissa of the amplitude-frequency curve of the compound biaxial system, and then the amplitude-frequency curve of the compound biaxial system is compared and analysed. The amplitude-frequency curves of the compound biaxial bearing for different eccentricities are shown in Figure 10.

Through the comparative analysis of the amplitude-frequency curves of different eccentricities, it is determined that when the "inner-outer" shaft of the compound biaxial system has an eccentricity, this will cause an unbalanced excitation of the system and additional external loads, resulting in the compound biaxial system resonating in the main excitation zone of the inner-outer axis, and changing the natural frequency and vibration characteristics of the system. Near the first-order critical speed, as the eccentricity of the inner shaft continues to increase, the amplitude-frequency of the main excitation area of the outer shaft is smaller, the resonance peak-peak response amplitude of the main excitation area of the inner shaft increases accordingly, and the critical speed of the system increases. Furthermore, as the eccentricity of the outer shaft continues to increase, the amplitude-frequency of the main excitation area of the inner shaft is smaller, the resonance peak-peak response amplitude of the main excitation area of the outer shaft increases accordingly, and the critical speed of the system increases. However, with the change in the amplitude of the abrupt points of acceleration and deceleration, the double steady-state interval (corresponding between the acceleration mutation point A and the deceleration mutation point B) of the compound biaxial does not change significantly.

Compared with not considering the effect of eccentricity, the vibration amplitude and its relative change are shown in Tables 5 and 6 under the condition of different eccentricity between the inner-outer axis. At the corresponding acceleration abrupt point A and deceleration abrupt point B, with the change of the eccentricity of the inner-outer axis, the amplitude of the main excitation zone changes significantly. In the acceleration and deceleration stages of the system, the relative changes of the inner axis and outer axis amplitudes are 17%–70% and 10%–130%, respectively. The system resonance peak in the main excitation region moves to the
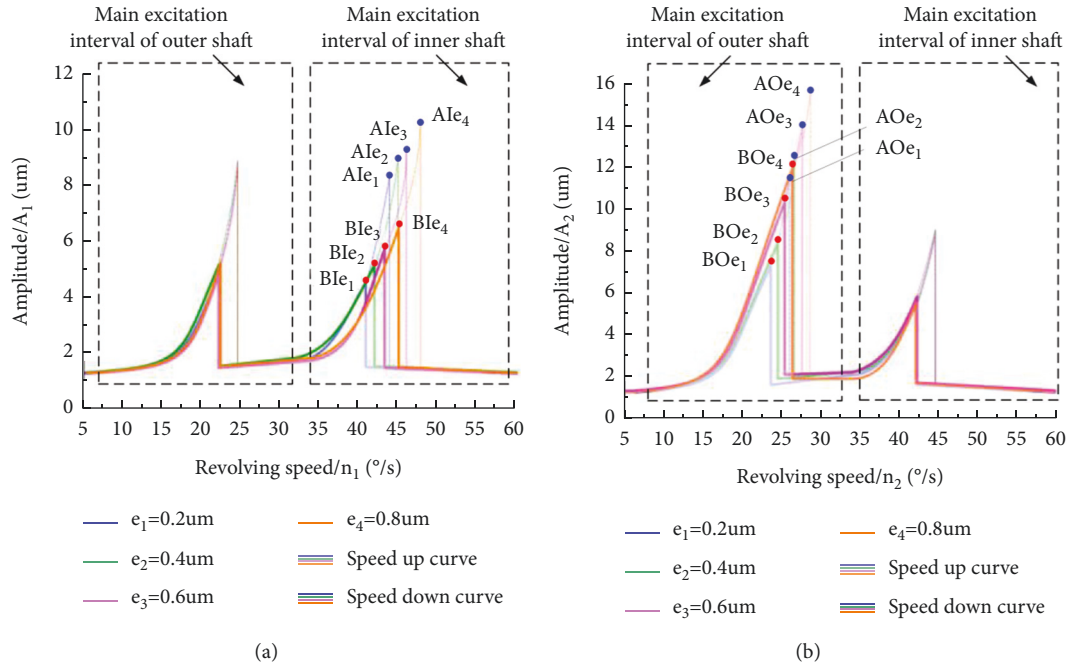
FIGURE 10: Amplitude-frequency curves of different eccentricities of shaft. Blue: eccentricities $0.2\,\mu$m; Green: eccentricities $0.4\,\mu$m; Pink: eccentricities $0.6\,\mu$m; Orange: eccentricities $0.8\,\mu$m (Corresponding excitation resonance peak, inner shaft: BIe_1, BIe_2, BIe_3, BIe_4, outer shaft: BOe_1, BOe_2, Boe_3, BOe_4). (a) Inner shaft. (b) Outer shaft.

TABLE 5: Vibration amplitude and its relative change for inner shaft.

Eccentricity (μm)	Speed up		Speed down	
	Amplitude (μm)	Relative change (%)	Amplitude (μm)	Relative change (%)
0.2	8.42	17.76	4.62	10.80
0.4	8.93	23.17	5.23	25.42
0.6	9.31	28.41	5.89	41.01
0.8	10.28	41.79	6.56	57.73

TABLE 6: Vibration amplitude and its relative change for outer shaft.

Eccentricity (μm)	Speed up		Speed down	
	Amplitude (μm)	Relative change (%)	Amplitude (μm)	Relative change (%)
0.2	11.43	24.92	7.32	39.96
0.4	12.35	34.97	8.36	59.85
0.6	13.92	52.13	10.34	97.71
0.8	15.56	70.05	12.01	129.64

high frequency about $8\,\mu$m–$16\,\mu$m and $4\,\mu$m–$12\,\mu$m, respectively, and the overall response trend of the inner-outer axis is consistent.

4.3. Amplitude-Frequency Response Analysis of Nonlinear Factors of Inter-Shaft Bearing.
The inter-shaft bearing is a key component to connect and support the "inner-outer" shaft, and it is also a main reason for the additional coupled vibration of the compound biaxial system. Therefore, it is very important to analyse the influence of the structural parameters (stiffness and radial clearance) of the inter-shaft bearing on the vibration characteristics of the system [23].

The influences of the different stiffnesses of the inter-shaft bearing on the amplitude-frequency response of the compound biaxial system are analysed, and the dynamic stiffnesses of the inter-shaft bearing are KH1 = 0.8 KH0, KH2 = KH0, and KH3 = 1.2 KH0. The amplitude-frequency curves of the different stiffnesses of the inter-shaft bearing regardless of the influence of the dynamic load of the system are shown in Figure 11.

Through the comparative analysis of the amplitude-frequency curves of the different stiffnesses, the change in the stiffness of the inter-shaft bearing of the compound biaxial system causes the bearing reaction force and the change of the contact deformation of the bearing balls and
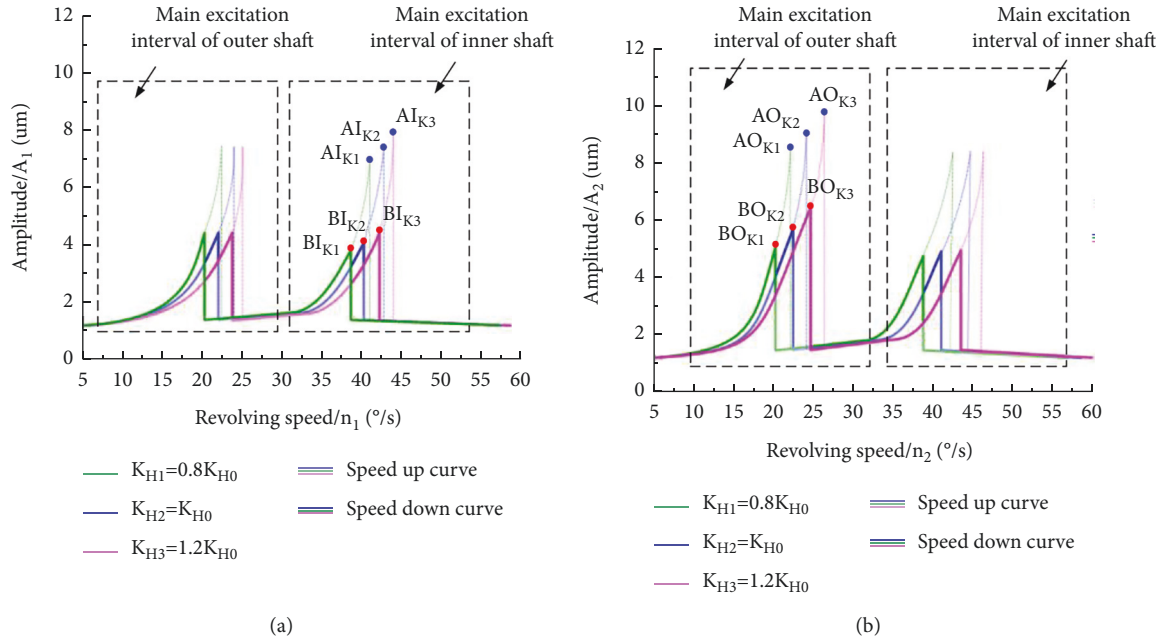
(a)

(b)

FIGURE 11: Amplitude-frequency curves of different stiffnesses of the inter-shaft bearing. Green: The coefficient of stiffness is 0.8. Blue: The coefficient of stiffness is 1. Pink: The coefficient of stiffness is 1.2 (Corresponding excitation resonance peak, inner shaft: BI_{K1}, BI_{K2}, BI_{K3}, outer shaft: BO_{K1}, BO_{K2}, BO_{K3}). (a) Inner shaft. (b) Outer shaft.

the inner-outer ring raceway, which in turn changes the natural frequency and vibration characteristics of the compound biaxial system. Near the first-order critical speed, the change of the stiffness of the inter-shaft bearing has little effect on the amplitude-frequency effect of the inner shaft in the main excitation zone of the outer shaft. However, with the increase of the stiffness of the inter-shaft bearing, the resonance peak-peak value of the inner shaft in the main excitation zone of the inner shaft increases accordingly, with the increasing of the speed corresponding to the peak value, and the critical speed of the system also increases. In addition, the change of the stiffness of the inter-shaft bearing has little effect on the amplitude-frequency effect of the outer shaft in the main excitation zone of the inner shaft. However, with the increase of the stiffness of the inter-shaft bearing, the resonance peak-peak value of the outer shaft in the main excitation zone of the outer shaft increases accordingly, with the increasing of the speed corresponding to the peak value, and the critical speed of the system also increases. At the same time, with the change of the amplitude of the abrupt points of the acceleration and deceleration, the double steady-state interval (Corresponding between the acceleration mutation point A and the deceleration mutation point B) of the compound biaxial decreases with the increase of the stiffness.

Compared with not considering the different stiffnesses of the inter-shaft bearing, the vibration amplitude and its relative change are shown in Tables 7 and 8 under the condition of different stiffnesses of the inter-shaft bearing. At the corresponding acceleration abrupt point A and deceleration abrupt point B, with the change of different stiffnesses of the inter-shaft bearing, the amplitude of the

main excitation zone changes significantly. In the acceleration and deceleration stages of the system, the relative changes of the inner axis and outer axis amplitudes are 4%–18% and 5%–8%, respectively. The system resonance peak in the main excitation region moves to the high frequency about $5\,\mu m$–$8\,\mu m$, and the overall response trend of the inner-outer axis are consistent.

In order to analyse the influence of the different radial clearances of the inter-shaft bearing on the amplitude-frequency response of the compound biaxial system, the radial clearances of the inter-shaft bearing are taken as $\delta 1 = 2\,\mu m$, $\delta 2 = 4\,\mu m$, and $\delta 3 = 6\,\mu m$. The amplitude-frequency curves of the different radial clearances of the inter-shaft bearing without the influence of the dynamic load of the system are shown in Figure 12.

Through the comparative analysis of the amplitude-frequency curves of the different radial clearances of the inter-shaft bearing, the change of the radial clearance of the inter-shaft bearing of the compound biaxial system causes the changes of the bearing reaction force and the time of the double-shaft contact, which leads to different coupling vibrations between the "inner-outer" shaft and the inter-shaft bearing, which in turn changes the natural frequency and vibration characteristics of the compound biaxial system. Near the first-order critical speed, the change of the radial clearance of the inter-shaft bearing has little effect on the amplitude-frequency effect of the inner shaft in the main excitation zone of the outer shaft. However, as the radial clearance of the inter-shaft bearing increases, the resonant peak-peak value of the main excitation zone of the inner shaft increases accordingly, with the speed corresponding to the peak value decreasing accordingly, and the critical speed

TABLE 7: Vibration amplitude and its relative change for inner shaft.

Stiffness K_H	Speed up		Speed down	
	Amplitude (μm)	Relative change (%)	Amplitude (μm)	Relative change (%)
0.8	6.93	4.41	3.92	5.60
1.0	7.25	0	4.17	0
1.2	7.91	9.10	4.48	7.43

TABLE 8: Vibration amplitude and its relative change for outer shaft.

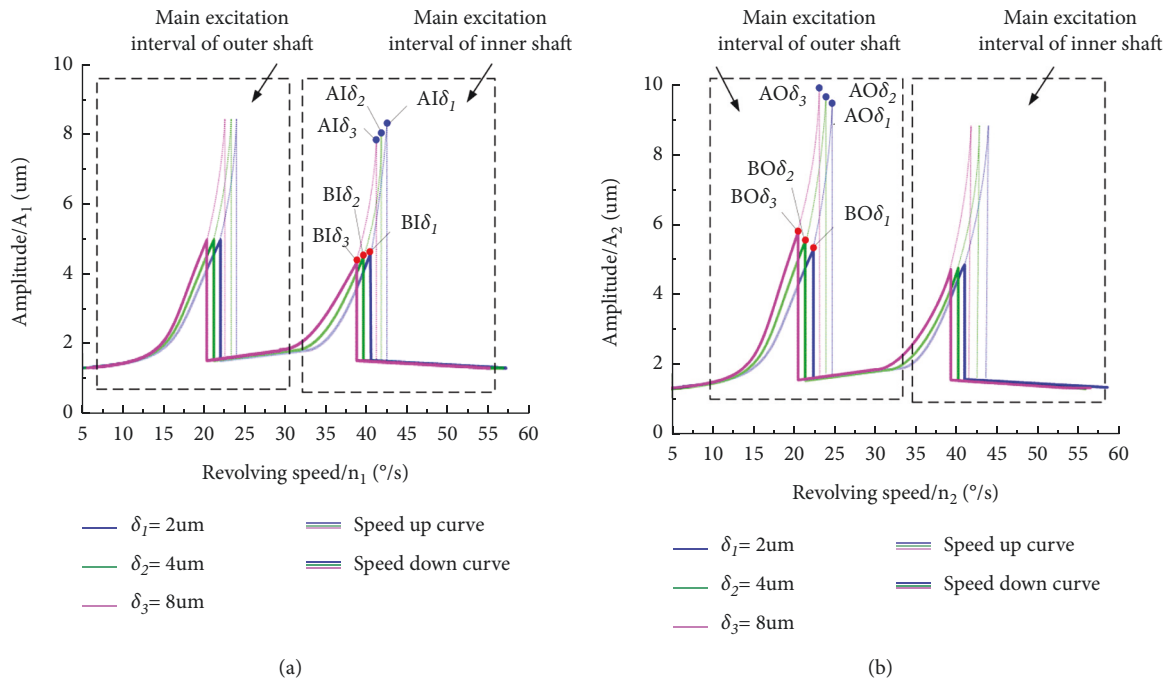| Stiffness K_H	Speed up		Speed down	
	Amplitude (μm)	Relative change (%)	Amplitude (μm)	Relative change (%)
0.8	5.01	4.21	8.60	6.01
1.0	5.32	0	9.15	0
1.2	6.25	17.48	9.88	7.39

FIGURE 12: Amplitude-frequency curves of different radial clearances of the inter-shaft bearing. Blue: radial clearance 2 μm; Green: radial clearance 4 μm; Pink: radial clearance 8 μm (Corresponding excitation resonance peak, inner shaft: $BI_{\delta 1}$, $BI_{\delta 2}$, $BI_{\delta 3}$, outer shaft: $BO_{\delta 1}$, $BO_{\delta 2}$, $BO_{\delta 3}$). (a) Inner shaft. (b) Outer shaft.

decreases accordingly. In addition, the change of the radial clearance of the inter-shaft bearing has little effect on the amplitude-frequency effect of the outer shaft in the main excitation zone of the inner shaft. However, with the increase of the radial clearance of the inter-shaft bearing, the resonant peak-peak value of the main excitation zone of the outer shaft increases accordingly, with the speed corresponding to the peak value correspondingly decreasing, and the critical speed of the speed therefore decreases. At the same time, with the change of the amplitude of the abrupt points of the acceleration and deceleration, the double steady-state interval (Corresponding between the acceleration mutation point A and the deceleration mutation point B) of the compound biaxial increases with the increase of the radial clearances.

Compared with not considering the different radial clearances of the inter-shaft bearing, the vibration amplitude and its relative change are shown in Tables 9 and 10 under the condition of different radial clearances of the inter-shaft bearing. At the corresponding acceleration abrupt point A and deceleration abrupt point B, with the change of different radial clearances of the inter-shaft bearing, the amplitude of the main excitation zone changes significantly. In the acceleration and deceleration stages of the system, the relative changes of the inner axis and outer axis amplitudes are 3%–15% and 4%–12%, respectively. The system resonance peak in the main excitation region moves to the high frequency about 5 μm–8 μm and 4 μm–10 μm, respectively, and the overall response trend of the inner-outer axis are consistent.

TABLE 9: Vibration amplitude and its relative change for inner shaft.

Radial clearance (μm)	Speed up		Speed down	
	Amplitude (μm)	Relative change (%)	Amplitude (μm)	Relative change (%)
2	8.32	14.46	4.65	11.51
4	7.98	10.07	4.56	9.35
8	7.72	6.48	4.35	4.32

TABLE 10: Vibration amplitude and its relative change for outer shaft.

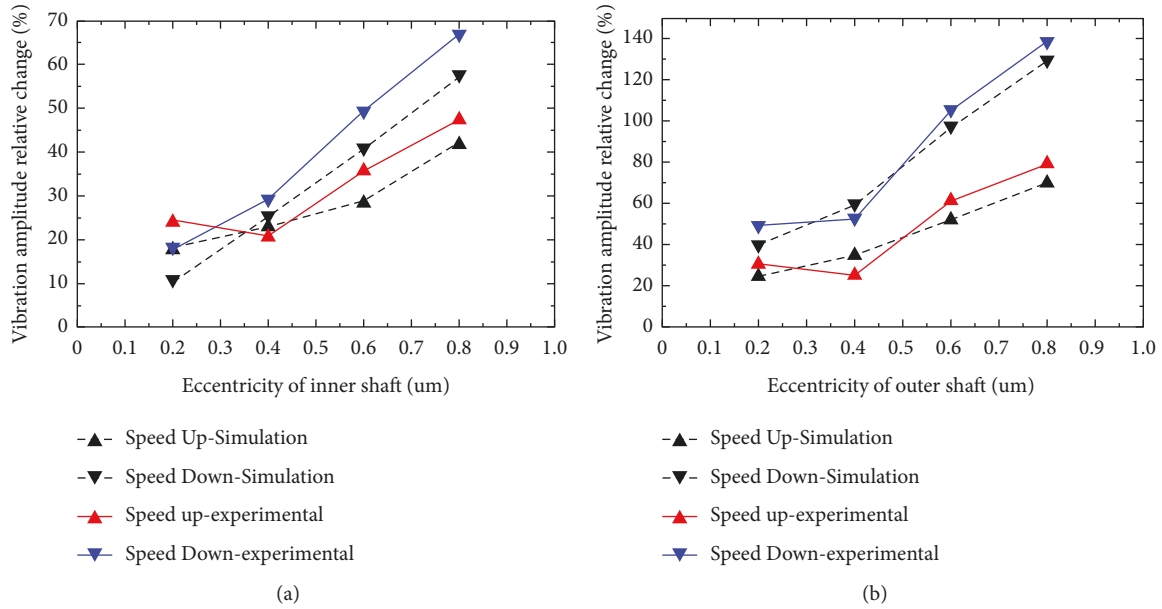| Radial clearance (μm)	Speed up		Speed down	
	Amplitude (μm)	Relative change (%)	Amplitude (μm)	Relative change (%)
2	5.41	3.44	9.52	4.04
4	5.62	7.46	9.75	6.56
8	5.93	13.38	9.96	8.85

(a)

(b)

FIGURE 13: Comparison curves of the vibration amplitude relative change for inner shaft and outer shaft. Red line: Speed up-experimental curve; Blue line: Speed down-experimental curve; Black line: the simulation curves of the Speed up and Speed down.

5. Experimental Verification

In order to verify the effectiveness of the numerical calculation for the coupling system model with the compound biaxial vibration characteristics, in this research, a scanning laser vibrometer PSV-500-1D combined with a single-point laser vibrometer OFV-5000 is used to carry out modal tests on the vibration characteristics of the compound biaxial system with different eccentricity (see Figure 7). In order to maximally approach the ideal working condition, the possible influencing factors are strictly controlled. The experimental test is carried out under laboratory conditions with constant temperature and humidity (temperature $20 \pm 1°$C, relative humidity 50 ± 5%) and relatively excellent vibration isolation conditions, the eccentric distance between the inner shaft and the outer shaft is strictly adjusted by a dial indicator. The excitation is applied to the end of the biaxial

structure by using the turntable control system, combined with the reference signal of the single-point laser vibrometer OFV-5000. The recording and the display of the data are achieved with a PSV-500-DMS data acquisition system, and compared with the numerical calculation results. The numerical calculation and experimental conditions (see Figure 13) are compared. The relative changes of the inner axis and outer axis amplitudes in the speed up and speed down stages are within the range of eccentricity 0–$1\,\mu$m, the maximum error of the relative changes of the system amplitude is less than 9.4%. The experimental and numerical results of the vibration characteristics of the compound biaxial system with different eccentricity are in good agreement, and the experimental results are reliable, which verifies the effectiveness of the dynamic numerical simulation analysis of the coupling system model with the compound biaxial structure.

6. Conclusions

In this research, the coupling system model of compound biaxial and inter-shaft bearings is established based on the theory of rotor dynamics and bearing contact deformation. Based on the consideration of the moment of inertia, gyro effect, and structural damping, the rationality of the coupling system model is verified through the analysis of the 1D beam model, the simulation of the 3D model, and the modal test for the coupling system. The amplitude-frequency characteristics are solved with consideration for the eccentricity of the compound biaxial and the nonlinear effects of the stiffness and radial clearance of the inter-shaft bearing, and the vibration characteristics of the compound biaxial and inter-shaft bearing coupling system are comprehensively analysed. The main conclusions are as follows:

(1) There are two excitation resonances and resonance mutations in the coupling system of the compound biaxial and inter-shaft bearings during the acceleration and deceleration phases, correspondingly forming the double steady-state interval of the speed near the first-order critical speed. The overall trends of the amplitude-frequency curve for the stages of the acceleration and deceleration are consistent.

(2) With the continuous increase of the eccentricity of the compound biaxial bearing, the amplitude of the main excitation zone corresponding to the "inner-outer" shaft increases near the first-order critical speed, and the critical speed increases, but the double steady-state interval of the speed is unchanged.

(3) With the continuous increase of the rigidity of the inter-shaft bearing, the supporting reaction force of the bearing increases, and the deformation of the contact becomes larger. The position of the first-order resonance peak of the system moves back, the critical speed increases, the amplitude increases, and the double steady-state interval of the speed decreases. At the same time, as the radial clearance of the inter-shaft bearing continues to increase, the supporting reaction force of the bearing decreases, the amount of contact deformation becomes smaller, and the contact time between the ball and the raceway is delayed. The position of the first-order resonance peak of the system moves forward, the critical speed decreases, the amplitude decreases, and the double steady-state interval of the speed increases.

(4) With the changes of the eccentricity of the compound biaxial bearing, the amplitude of the main excitation zone corresponding to the system changes significantly, and the resonance peak-peak response amplitude of the main excitation area of the system moves about $4\,\mu$m–$16\,\mu$m to the high frequency, and the relative changes of the inner axis and outer axis amplitudes are 10%–130%. As the stiffnesses and the radial clearances of the inter-shaft bearing change, the amplitude of the main excitation zone corresponding to the system changes obviously, the resonance peak-peak response amplitude of the main excitation area of the system moves about $4\,\mu$m–$10\,\mu$m to the high frequency, but the relative changes of the inner axis and outer axis amplitudes are 3%–18%.

Due to the change of the eccentricity of the compound biaxial bearing and the structural parameters of the inter-shaft bearing, the unbalanced excitation and the additional external load of the compound biaxial system are caused, as well as the change of the contact deformation between the balls and the raceway of the inter-shaft bearing, which leads to the resonance of the compound biaxial system in the main excitation zone, and there is a different coupling vibration between the shaft and the bearing. Therefore, combined with the coupling system model and vibration characteristics of the compound biaxial structure and the inter-shaft bearing, the structural parameters and the dynamic characteristics of the system are reasonably optimized, which can effectively suppress the resonance of the system.

Data Availability

The data used to support the findings of this study are included within the article.

Conflicts of Interest

The authors declare that there are no conflicts of interest regarding the publication of this paper.

Acknowledgments

References

[1] K. Li, H. Ding, G. Cao, H. Hou, and C. Zhao, "Research on high-precision error measurement system of angular displacements based on reciprocal roll angles," *Optical Engineering*, vol. 59, no. 12, pp. 1–17, Article ID 124110, 2020.

[2] M. Huang, Q. Xu, M. Li, B. Wang, and J. Wang, "A calculation method on the performance analysis of the thrust aerostatic bearing with vacuum pre-load," *Tribology International*, vol. 110, no. 2, pp. 125–130, 2017.

[3] M. Huang, P.-K. Liu, Y.-Q. Xia, M.-Y. Li, and Q. Tang, "Calibration of circular division artifacts using a self-developed angle comparator," *Optics and Precision Engineering*, vol. 27, no. 1, pp. 110–120, 2019.

[4] H. Yu, X.-R. Lu, C.-H. Zhao, and L.-H. Liang, "Calibration of dynamic precision for measurement platform of photoelectric encoder," *Optics and Precision Engineering*, vol. 24, no. 11, pp. 2699–2704, 2016.

[5] H. Zhang, Z. Chen, W. Cheng, and Y. Zhao, "Vibration characteristics analysis of joint with multiple clearances in space mechanism," *Journal of Mechanical Engineering*, vol. 53, no. 11, pp. 44–53, 2017.

 [6] Y. Liu, J. Wang, and L. Chen, "Rub-impact vibration analysis of PH/LH turbines of aeroengine dual-rotor system," *Journal of Vibration and Shock*, vol. 10, no. 1, pp. 243–253+263, 2021.

 [7] T. Zhang and J. Cui, "Analytical method for fluid-solid coupling vibration analysis of hydraulic pipeline system with hinged ends," *Shock and Vibration*, vol. 7, Article ID 8846869, 2021.

 [8] N. Wang, D. Jiang, and H. Xu, "Dynamic characteristics analysis of a dual-rotor system with inter-shaft bearing," *Proceedings of the Institution of Mechanical Engineers - Part G: Journal of Aerospace Engineering*, vol. 233, no. 3, pp. 1147–1158, 2019.

 [9] G. Nan, Y. Zhu, Y. Zhang, and W. Guo, "Nonlinear dynamic analysis of rotor-bearing system with cubic nonlinearity," *Shock and Vibration*, vol. 5, Article ID 8878319, 2021.

[10] Z. Yu and Y. Zhang, "Diagnosis of the misaligned faults of the vertical test instrument of high-precision industrial robot reducer," *Shock and Vibration*, vol. 7, Article ID 5516025, 2021.

[11] H. Taplak and M. Parlak, "Evaluation of gas turbine rotor dynamic analysis using the finite element method," *Measurement*, vol. 45, no. 5, pp. 1089–1097, 2012.

[12] M. H. Jalali, M. Ghayour, S. Ziaei-Rad, and B. Shahriari, "Dynamic analysis of a high speed rotor-bearing system," *Measurement*, vol. 53, pp. 1–9, 2014.

[13] E. Chatelet, F. D'Ambrosio, and G. Jacquet-Richardet, "Toward global modelling approaches for dynamic analyses of rotating assemblies of turbomachines," *Journal of Sound and Vibration*, vol. 282, no. 2, pp. 163–178, 2005.

[14] H. Ma, Y. Lu, Z. Wu, X. Tai, H. Li, and B. Wen, "A new dynamic model of rotor-blade systems," *Journal of Sound and Vibration*, vol. 357, pp. 168–194, 2015.

[15] Y.-J. Chiu and D.-Z. Chen, "The coupled vibration in a rotating multi-disk rotor system," *International Journal of Mechanical Sciences*, vol. 53, no. 1, pp. 1–10, 2011.

[16] M. Wang, Q. Han, B. Wen, H. Zhang, and T. Guan, "Modal characteristics and unbalance responses of fan rotor system with flexible support structures in aero-engine," *Proceedings of the Institution of Mechanical Engineers - Part G: Journal of Aerospace Engineering*, vol. 231, no. 9, pp. 1686–1705, 2017.

[17] S. M. Jeon, H. D. Kwak, S. H. Yoon, and J. Kim, "Rotordynamic analysis of a high thrust liquid rocket engine fuel (Kerosene) turbopump," *Aerospace Science and Technology*, vol. 26, no. 1, pp. 169–175, 2013.

[18] Y. Liu, J. Wang, and L. Chen, "Cross coordinate system modelling method for a dual-rotor system with initial bending of its low-pressure rotor," *Journal of Vibration and Shock*, vol. 39, no. 3, pp. 60–68+75, 2020.

[19] R. Whalley and A. Abdul-Ameer, "Contoured shaft and rotor dynamics," *Mechanism and Machine Theory*, vol. 44, no. 4, pp. 772–783, 2008.

[20] B. Qiao, D. Zhang, and M. Yu, "Analysis on vibration of intershaft bearing with inner and outer ring rotating in same and opposite direction," *Bearing*, vol. 1, pp. 52–55, 2018.

[21] M. Du, Y. Hou, and Y. Wu, "Synchronization behavior of two Co-rotating rotors in a nonlinear coupled system," *Journal of Mechanical Engineering*, vol. 56, no. 23, pp. 150–164, 2020.

[22] C. Jarroux, J. Mahfoud, R. Dufour, F. Legrand, B. Defoy, and T. Alban, "Investigations on the dynamic behaviour of an on-board rotor-AMB system with touchdown bearing contacts: modeling and experimentation," *Mechanical Systems and Signal Processing*, vol. 159, Article ID 107787, 2021.

[23] S. Li, F. Liu, and H. Wang, "Nonlinear vibration analysis of rotor considering cogging and harmonic effects," *Shock and Vibration*, vol. 3, Article ID 6685588, 2021.